LANGMUIR

pubs.acs.org/Langmuir Article

Temperature-Induced Aggregation in Portlandite Suspensions

Sharu Bhagavathi Kandy, Iman Mehdipour, Narayanan Neithalath, Mathieu Bauchy, Edward Garboczi, Samanvaya Srivastava, Torben Gaedt, and Gaurav Sant*

Cite This: *Langmuir* 2020, 36, 10811−10821 Read Online

ACCESS | Metrics & More | Article Recommendations | Supporting Information

ABSTRACT: Temperature is well known to affect the aggregation behavior of colloidal suspensions. This paper elucidates the temperature dependence of the rheology of portlandite (calcium hydroxide: $Ca(OH)_2$) suspensions that feature a high ionic strength and a pH close to the particle's isoelectric point. In contrast to the viscosity of the suspending medium (saturated solution of $Ca(OH)_2$ in water), the viscosity of $Ca(OH)_2$ suspensions is found to increase with elevating temperature. This behavior is shown to arise from the temperature-induced aggregation of polydisperse $Ca(OH)_2$ particulates because of the diminution of electrostatic repulsive forces with increasing temperature. The temperature dependence of the suspension viscosity is further shown to diminish with increasing particle volume fraction as a result of volumetric crowding and the formation of denser fractal structures in the suspension. Significantly, the temperature-dependent rheological response of suspensions is shown to be strongly affected by the suspending medium's properties, including ionic strength and ion valence, which affect aggregation kinetics. These outcomes provide new insights into aggregation processes that affect the temperature-dependent rheology of portlandite-based and similar suspensions that feature strong charge screening behavior.

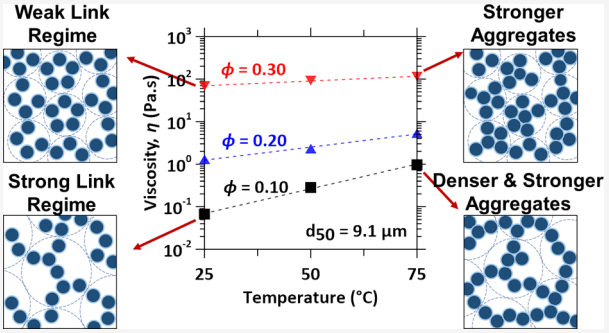

Downloaded via UNIV OF CALIFORNIA LOS ANGELES on September 30, 2020 at 06:30:47 (UTC).
See https://pubs.acs.org/sharingguidelines for options on how to legitimately share published articles.

INTRODUCTION

Controlling the flow behavior of dense suspensions is relevant to the industrial processing of colloidal and particulate suspensions.[1] Because of their unique structural and mechanical properties, dense suspensions feature in diverse areas including the formulation of food,[2,3] wet processing of ceramics,[4−7] paints and coatings,[1] drilling fluids,[8] and advanced inks for 3D printing.[7,9−13] Often, these suspensions exhibit non-Newtonian flow behaviors including non-zero yield stress, shear thinning, and shear thickening[14] that are strongly affected by the size, shape, and volume fraction of the solid particles,[15−17] colloidal stability, and the fractal structuring of the particle aggregates.[18,19] Colloidal stability and the structure of the aggregates are intimately dictated by the nature of the underlying interparticle interactions. The suspending medium's attributes such as ionic strength, pH, and counterion valence can be crucial in controlling interparticle interactions as they can modify particle surface chemistry and solid−fluid interfacial chemistry.[20,21] The elaboration of correlations between the microscopic interparticle interactions and the macroscopic rheological properties of suspensions, thus, continues to be of great engineering interest.[18,19,22−25]

Often, processing parameters such as temperature, pH, and ionic strength are tuned to alter the processability of dense suspensions by controlling their propensity for colloidal aggregation and, in turn, the resulting rheology. Temperature, in particular, is of crucial relevance in applications such as 3D printing, deep well cementing, and extrusion.[26−29] In strongly repulsive colloidal suspensions comprising well-dispersed particles, the temperature response of the suspension viscosity is primarily controlled by the temperature dependence of the viscosity of the suspending medium.[30,31] Consequently, the activation energy of viscous flow—that is, the temperature dependence of suspension viscosity—is often independent of the solid volume fraction and the shear rate.[30] The temperature dependence of the rheology of suspensions that feature attractive or weakly repulsive particles, however, is more complex because temperature induces changes in particle to particle and particle to suspending-medium interactions.[32,33] In addition to impacting Brownian motion, temperature affects attributes including solubility of the solid phase, pH of the suspending medium, particle surface potential, and viscosity and dielectric properties of the suspending medium.[29,34] These effects can notably impact particle aggregation, suspension stability, and rheology.[35−39] For instance, the apparent viscosity was found to increase with increasing temperature in flocculated suspensions of alumina,[40] silicon carbide,[34]

Received: June 17, 2020
Revised: August 14, 2020
Published: August 17, 2020

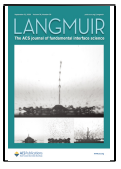

© 2020 American Chemical Society

https://dx.doi.org/10.1021/acs.langmuir.0c01798
Langmuir 2020, 36, 10811−10821

zirconia,[41] and iron oxide[42] particles. In these suspensions, an increase in temperature was thought to induce accelerated aggregation, leading to a higher resistance to shear-driven flow, despite the reduction in the viscosity of the suspending medium.

However, the mechanisms by which temperature affects the structure of aggregating colloidal suspension and, in turn, how their structure governs rheology remain unclear. Herein, we elaborate on these mechanisms through detailed analyses of the temperature−structure−rheology response of $Ca(OH)_2$ suspensions that feature varying solid volume fractions and broad aggregated particle size distributions. We focus on calcium hydroxide ($Ca(OH)_2$, also known as portlandite and slaked or hydrated lime), given its wide applications in the food industry,[3] architecture and decorative arts,[43] water treatment,[44,45] dentistry,[46] and carbon dioxide mineralization.[47,48] The role of ionic strength and ion valence of the suspending medium on temperature-dependent rheological response is particularly highlighted. Taken together, the work offers a new understanding that is needed to control the rheological properties of colloidal suspensions that feature strong charge screening behavior and specifically how to account for temperature changes that affect the engineering-scale processability of these suspensions.

MATERIALS AND METHODS

Materials. Two grades of commercially available portlandite powders (standard hydrated lime and Microcal HS obtained from Mississippi Lime, density = 2340 kg/m^3)[a] were used. The portlandite was of a purity of 94.8 ± 0.5% by mass as determined by thermogravimetric analysis (TGA), with the remainder being $CaCO_3$. Quartz particles (MINUSIL 5, U.S. Silica, density = 2650 kg/m^3) with a near-identical median particle size as that of standard hydrated lime was used as a *near-inert* mineral to examine the effects of the ionic strength and ion valence of the suspending aqueous medium. The particle size distributions of the powders were measured using static light scattering (SLS; LS13-320, Beckman Coulter) with saturated $Ca(OH)_2$ solution used as a carrier liquid. The median particle diameters (d_{50}) of the two portlandite particles (standard hydrated lime and Microcal HS) and quartz and their specific surface areas (estimated using the particle size distribution) were determined as 4.6 ± 0.1 μm (specific surface area: 1357 ± 16 m^2 kg^{-1}), 9.1 ± 0.1 μm (specific surface area: 711 ± 11 m^2 kg^{-1}), and 5.1 ± 0.2 μm (specific surface area: 535 ± 19 m^2 kg^{-1}), respectively, wherein the error represents the standard deviation based on three replicate measurements (see the Supporting Information, Figure S1a). It should be noted that the portlandite particulates consisted of aggregates of much smaller primary $Ca(OH)_2$ particles, as evidenced by field emission-scanning electron micrographs (FEI NanoSEM 230; see Figure S1b). The primary $Ca(OH)_2$ particle size was on the order of 20−200 nm (see Figure S1c), as determined using transmission electron microscopy (FEI T12 Quick CryoEM and CryoET). The aggregate size visualized using SEM was similar to that estimated using static light scattering.

To prevent the dissolution of $Ca(OH)_2$ particles, a saturated $Ca(OH)_2$ solution was used as the suspending medium to prepare the suspensions. In order to prepare the saturated $Ca(OH)_2$ solution, excess $Ca(OH)_2$ was added to deionized (DI) water. The solids were allowed to settle for 24 h in a sealed container, and the solution was thereafter filtered using a 0.20 μm syringe filter. Portlandite suspensions were prepared at varying solid volume fractions (ϕ) ranging between 0.10 and 0.32, and their rheological properties were examined over a temperature range from 25 to 75 °C. To prepare suspensions of the selected volume fraction, the corresponding weight of $Ca(OH)_2$ particulates was estimated based on the bulk density and added to the saturated $Ca(OH)_2$ solution. The mixture was stirred for 300 s using a four-blade impeller-type mixer (RW 20 Digital, IKA) at 500 rpm. It should be noted that portlandite suspensions feature pH self-regulation (pH 12.6, isoelectric point: pH 13) and a relatively high ionic strength (~60 mM),[49] which results in the spontaneous aggregation of $Ca(OH)_2$ particles in suspension.[50] For the quartz suspensions, different suspending media having different ionic strengths were produced by dissolving the required amount of $Ca(OH)_2$ in DI water.

Rheology. The rheological properties of the suspensions were assessed for a range of particle solid volume fractions of portlandite and quartz at various temperatures using a combined motor-transducer rheometer (Discovery HR-2, TA Instruments), which was equipped with a Peltier concentric cylinder jacket for temperature control. A four-bladed vane in the cup geometry was used to perform the rotational steady-state shear rate sweep and small-amplitude oscillatory shear rheology analyses on suspensions, which were conditioned to three different temperatures (T = 25 ± 0.1 °C, T = 50 ± 0.1 °C, and T = 75 ± 0.1 °C). To limit the evaporation of water from the suspension during testing, the sample was enclosed by a solvent trap that was surrounded by a wet sponge. Following loading, the sample was initially conditioned at 25 ± 0.1 °C and held for 180 s before initiating the measurement to minimize temperature gradients. Following the temperature equilibration, the suspensions were subjected to preshear for 60 s at shear rate $\dot{\gamma}$ = 100 s^{-1} to homogenize the suspension and to eliminate shear history effects. The shear rate was then reduced to 0.001 s^{-1} and was held constant for 10 s for the initial relaxation. A reversible (ascending−descending) shear rate sweep procedure was applied in logarithmic steps (six points per decade) from $\dot{\gamma}$ = 0.001−100 s^{-1} with a 10 s data-averaging period. To assess the viscoelastic behavior and elasticity of aggregates in the suspension, small-amplitude oscillatory shear (SAOS) rheology was conducted on samples conditioned at varying temperatures. Following the steady-state shear rate experiment at each temperature, a similar preshearing regime was used—however, a longer rest time of 300 s was employed to enable the suspension to rebuild its structure before the amplitude sweep. A shear-strain amplitude (γ) sweep from γ = 0.001% to γ = 1000% was performed at a fixed frequency of 1 Hz.

Prior to rheological measurements at varying temperatures, an adequate waiting time (≈30 min) was applied for the sample in the cup to ensure that it reached the set temperature that was verified using a thermocouple probe (OMEGA). Following measurements at different temperatures, an additional test at 25 ± 0.1 °C was performed on the cooled-down suspension after an equilibration time of 30 min (i.e., the time required to lower temperature from 75 to 25 °C) to assess the irreversibility of the rheological response because of the imposed temperature variations. It should be noted that the results of temperature-dependent rheological properties were not affected by water evaporation and/or carbonation of $Ca(OH)_2$ particles (i.e., the reaction of portlandite with atmospheric CO_2 to produce solid calcium carbonates) over the course of measurements. The former was verified by determining the water content of the suspension at the end of the test and compared with the amount of water added initially, while the latter was verified by measuring the extent of carbonation before and after rheology measurements using TGA (STA 6000, Perkin Elmer).

Dynamic Light Scattering. Dynamic light scattering (DLS) analysis of suspended $Ca(OH)_2$ and quartz particles were carried out using a Zetasizer Nano ZS (Malvern Instruments Ltd., U.K.) to assess the floc size (and in turn, aggregation kinetics) at 25, 50, and 70 °C. The instrument was equipped with a helium−neon laser source (633 nm), 173° detection optics, and built-in Peltier temperature control with an accuracy of ±0.1 °C. DLS measurements were carried out on less-concentrated suspensions (ϕ = 0.002%[b]) of particles in saturated $Ca(OH)_2$ solutions that were sonicated for 20 min prior to the measurements. The normalized "Z-average" size (i.e., the average intensity-based floc size) of particle aggregates was recorded at 5 min intervals up to 60 min to trace the aggregation kinetics and floc size evolution.

Zeta Potential. The zeta potential (ζ, mV) of the particles in suspension was determined at 25, 50, and 70 °C using a Zetasizer Nano ZS (Malvern Instruments Ltd. U.K). The measurements were

https://dx.doi.org/10.1021/acs.langmuir.0c01798
Langmuir 2020, 36, 10811−10821

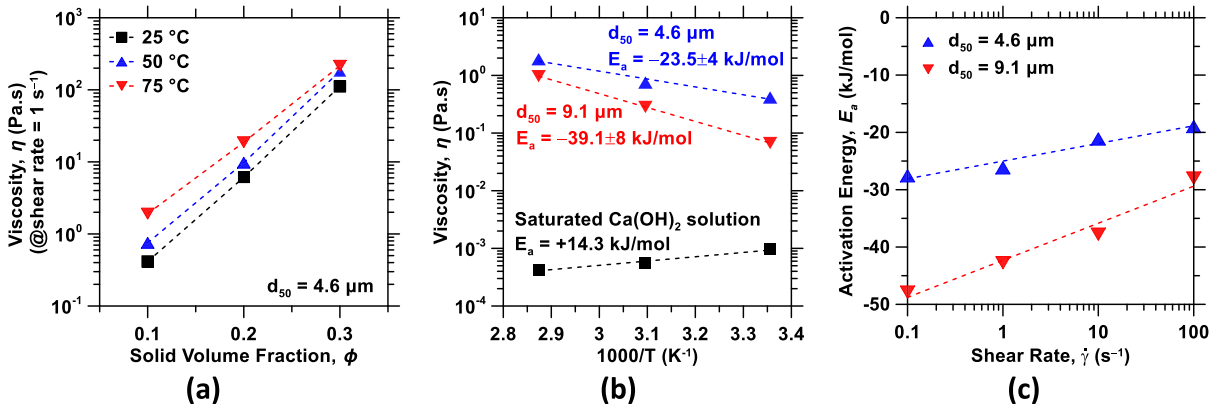

Figure 1. (a) Apparent viscosity trends of $Ca(OH)_2$ suspensions (for d_{50} = 4.6 μm) at a shear rate of $\dot{\gamma}$ = 1 s^{-1} as a function of the solid volume fraction at 25, 50, and 75 °C. Based on three replicate measurements, the uncertainty in the measured apparent viscosity data is <12%; (b) representative Arrhenius plots of apparent viscosity for saturated $Ca(OH)_2$ solutions and $Ca(OH)_2$ suspensions with ϕ = 0.1 at $\dot{\gamma}$ = 1 s^{-1}. The data were fitted using an Arrhenius-like equation. The error represents the standard deviation of E_a across different shear rates (see Figure S4); (c) variations in the apparent activation energy of viscous flow as a function of shear rate for $Ca(OH)_2$ suspensions with ϕ = 0.1.

carried out on dilute suspensions (ϕ = 0.002%) of portlandite particles in saturated $Ca(OH)_2$ solutions. For quartz, the suspensions were composed of varying ionic strengths. The zeta potential values are estimated from the measured electrophoretic mobilities using Henry's equation with the Smoluchowski approximation.[51]

RESULTS AND DISCUSSION

Temperature Dependence of Suspension Rheology. Calcium hydroxide ($Ca(OH)_2$) suspensions exhibited an increase in viscosity with increasing temperature (Figure 1a). This atypical temperature-dependent viscosity response was noted for different suspensions consisting of particles with two size distributions (d_{50} = 4.6 μm and d_{50} = 9.1 μm) at different solid volume fractions (ϕ = 0.1, ϕ = 0.2, and ϕ = 0.3), for a total of six possible suspensions (Figures 1a and S3, respectively). Similar to the viscosity response, $Ca(OH)_2$ suspensions exhibited an increase in yield stress and elastic modulus with increasing temperature (see Figure S6 in the Supporting Information). Contrastingly, in the absence of solid particles, the viscosity of a $Ca(OH)_2$ saturated solution decreased from 0.96 to 0.42 mPa·s with increasing temperature from 25 to 75 °C. The temperature dependence of suspension viscosity at varying ϕ and particle sizes was described by the activation energy of viscous flow, E_a, by fitting the experimental data to an Arrhenius-like equation: $\eta = \eta_\infty \exp(E_a/RT)$, with η_∞, R, and T being the exponential prefactor, gas constant, and thermodynamic temperature, respectively (see Figure S4 in the Supporting Information).[33,42,52,53] It has been found that the exponential prefactor η_∞ (i.e., the fictitious viscosity at infinite temperature) depends on the suspending medium and the volume fraction of the suspended particles.[42] Based on this analysis, the temperature-dependent viscosity response of $Ca(OH)_2$ suspensions indicated anomalous "negative" viscous activation energies of E_a = −23.5 ± 4 kJ/mol and −39.1 ± 8 kJ/mol for suspensions with ϕ = 0.1 composed of particles of d_{50} = 4.6 and 9.1 μm, respectively (see Figure 1b). On the other hand, the saturated $Ca(OH)_2$ solution (i.e., ϕ = 0) exhibited a positive activation energy (E_a = +14.3 kJ/mol), similar to that of water, that is, E_a = +15 kJ/mol.[54] The reprecipitation of $Ca(OH)_2$ with increasing temperature causes a marginal increase in ϕ on account of its solubility reduction as temperature increases (solid volume fraction change $\Delta\phi \leq$ 0.02% from 25 to 75 °C). However, the positive activation energy of saturated $Ca(OH)_2$ solution suggests that the reprecipitation of $Ca(OH)_2$ with increasing temperature does not cause the significant increase in viscosity of portlandite suspensions.

A similar increase in viscosity with temperature has been observed in suspensions composed of alumina, silicon carbide, zirconia, and iron oxide particles.[34,40−42] Such a behavior has been typically attributed to the increasing propensity for particle aggregation with temperature. The negative value of the activation energy is often related to a transition of the suspension's microstructure toward a more aggregated state with increasing temperature.[55,56] The negative values of both the activation enthalpy and activation entropy imply that the formation of aggregates was enthalpically and entropically favored at elevated temperatures. The disparity between the apparent viscous activation energy of the suspensions and the corresponding saturated solutions indicates a coupling between the particle aggregation state and suspension rheology. An indication of this coupling is revealed via the shear rate dependence of the suspension viscosity. Typically, shearing suspensions at high $\dot{\gamma}$ breaks down aggregates, thus enhancing particle dispersion. This improved dispersion and shear-induced alignment of particle aggregates manifest itself as a reduction in the suspension viscosity, thereby resulting in shear-thinning behavior (see Figure S3 in the Supporting Information). In addition to a decrease in the viscosity with increasing $\dot{\gamma}$, a moderation of temperature sensitivity of the suspension viscosity is noticed with increasing $\dot{\gamma}$, and this can be ascribed to reduced particle aggregation and improved particle dispersion at high shear rates because of the breakup of aggregates under shear (Figure 1c).[57,58]

Particle aggregation results in an increase in yield stress and viscosity,[17,18,59,60] while the degree of agglomeration of particles in a suspension is primarily controlled by the dynamic equilibrium between the hydrodynamic forces induced by shear deformations and the colloidal interactions between the particles.[32,61] The Mason number, Mn, defined as a measure of the hydrodynamic force exerted on particle aggregates relative to the strength of attraction between contacting particles in the aggregates, is often used to describe the aggregate breakup under shear flow.[62,63] The Mason number is estimated as $Mn = 6\pi\eta_0\dot{\gamma}a^3/\Gamma$, where η_0 is the suspending fluid viscosity, a is the radius of the primary particle, $\dot{\gamma}$ is the imposed shear rate, and

https://dx.doi.org/10.1021/acs.langmuir.0c01798
Langmuir 2020, 36, 10811−10821

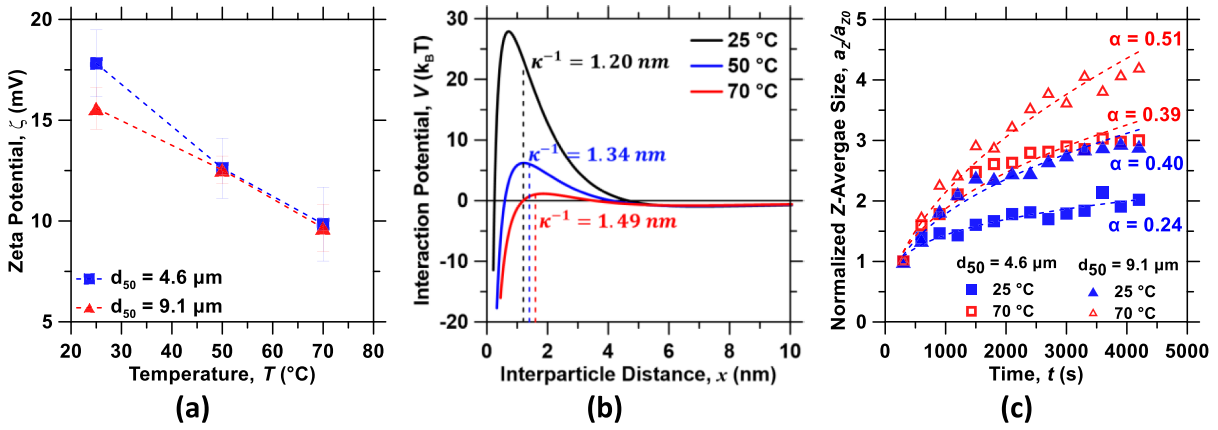

Figure 2. (a) Zeta potential of $Ca(OH)_2$ particles suspended in a saturated solution of $Ca(OH)_2$ as a function of temperature. (b) Sphere−sphere interparticle interaction potential calculated using DLVO theory as a function of the surface−surface separation distance for $Ca(OH)_2$ particles (a = 50 nm) suspended in a saturated $Ca(OH)_2$ solution at 25, 50, and 70 °C. The estimated interparticle potentials consider the ionic strength and zeta potential at each temperature. (c) Normalized "Z-average" size of $Ca(OH)_2$ aggregates at 25, 50, and 75 °C as determined by DLS measurements in dilute suspensions (0.05 g/L). The normalized "Z-average" data were obtained by dividing Z-average at time t to its initial reading. A highest uncertainty of ∼20% in the Z-average particle size was observed based on five replicate measurements. The dashed lines indicate power-law fits of the form $a_z \propto {}_{z_0} t a^{\alpha}$, where a_{z_0} is the initial floc size and α is a power-law exponent.

Γ is the strength of van der Waals attraction between the particles at contact.[62] The van der Waals attraction strength was estimated using nonretarded Hamaker pair potentials by assuming spherical primary particles of 100 nm diameter and a short attraction width of 0.5 nm. The suspensions under study were subjected to a steady shear rate sweep in the range $\dot{\gamma}$ = 10^{-3} −10^{2} s^{-1}, and the estimated variation in Mn is between 10^{-5} and 10^{1} (see Figure S3 in the Supporting Information). At small shear rates, Mn < 10^{-2}, shear forces inducing aggregate bond breakup are significantly smaller than attractive forces that hold the particles in the aggregates.[62] At sufficiently high shear rates, Mn > 1, shear forces are strong enough to break the aggregate network into individual components. At intermediate deformation rates, aggregate breakup and reformation of particle−particle bonds result in dynamic equilibrium and result in the evolution of flow heterogeneities and secondary structures.[64] It should be noted that the Mason number, as defined here, is ideally valid for spherical particles, and the critical value is system size-dependent. However, these limitations are not expected to fundamentally change the overall trends.

Thus, temperature-induced particle aggregation diminishes at higher deformation rates, and consequently, the estimated activation energy varies with the imposed $\dot{\gamma}$ (Figures 1c and S5). It suggests that, in the limit, as the particle aggregates are broken down to primary particles and, in the dilute limit (i.e., if the particles were separated sufficiently to be noninteracting), at infinitely high $\dot{\gamma}$, the apparent activation energy of the portlandite suspensions would converge to that of portlandite solutions (Figure 1c) to become positive. Furthermore, the larger-size $Ca(OH)_2$ particles (d_{50} = 9.1 μm) manifested a higher temperature sensitivity (Figure 1b) as compared to the smaller-size $Ca(OH)_2$ particles (d_{50} = 4.6 μm). This indicates that these somewhat larger particles aggregate more readily at higher temperatures. However, such larger aggregates, because they tend to be more-weakly cohered, break down more readily upon external shearing (Figure 1c). Furthermore, the viscous activation energy is also influenced by the solid volume fraction, and this dependence is discussed in the next section.

The effects of temperature on interparticle interactions were examined as follows. First, the reduced solubility of $Ca(OH)_2$ and its marginal precipitation with increasing temperature decreased both the pH and ionic strength (I) of the solution (see Figure S8 in the Supporting Information). The surface charge of the suspended $Ca(OH)_2$ particles is affected by Ca^{2+} ions in solution. Thus, the zeta potential (ζ) of $Ca(OH)_2$ particles also decreased with increasing temperature (Figure 2a). The decrease in ζ weakens electrostatic/Coulombic particle−particle repulsions, thereby increasing the electrokinetic instability and aggregation tendency. In turn, the decrease in I reduces the magnitude of electrostatic screening and increases the thickness of the electric double layer (EDL). To determine the competing effect between I and ζ on the net interaction potential energy between particles, DLVO (Derjaguin−Landau−Verwey−Overbeck) interactions were estimated by taking into account the temperature dependence of ionic strength and surface charge density. The interparticle interaction potential (V) as a function of the distance between the particle surfaces (x) was estimated following eq 1, which sums the electrostatic repulsion (V_{es}) and van der Waals attraction (V_{vdW}) components.[65−68] The component V_{es} was estimated using the Hogg−Healy−Fuerstenau interaction potential, which is based on the linearized Poisson−Boltzmann equation,[66] and V_{vdW} was estimated using nonretarded Hamaker pair potentials.[67] The DLVO interparticle interactions were simulated using the Hamaker 2.2 software package,[65] and calculations assumed a spherical geometry for particles with a primary particle diameter of 100 nm.

$$V(x) = V_{es}(x) + V_{vdW}(x) = 2\pi\varepsilon_r\varepsilon_0\psi^2 a \ln[1 + \exp(-\kappa x)] - \frac{A}{6}\left(\frac{2a^2}{x^2 + 4ax} + \frac{2a^2}{(x + 2a)^2} + \ln\left(\frac{x^2 + 4ax}{(x + 2a)^2}\right)\right) \quad (1)$$

where a is the primary particle radius, ε_r is the relative permittivity of the medium, ε_0 is the permittivity of vacuum, κ is the characteristic electrostatic decay length of an electric

https://dx.doi.org/10.1021/acs.langmuir.0c01798
Langmuir 2020, 36, 10811−10821

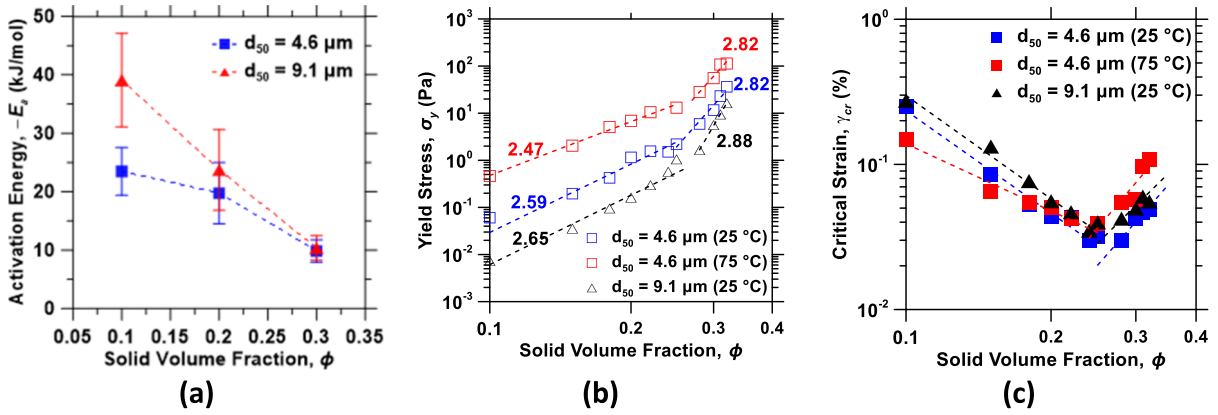

Figure 3. (a) Apparent activation energy of the viscous flow of $Ca(OH)_2$ suspensions as a function of the solid volume fraction. The error bars correspond to the variation in the estimated E_a for suspension viscosities over the entire shear rate range. (b) Critical yield stress σ_y of $Ca(OH)_2$ suspensions as a function of solid volume fraction ϕ at 25 and 75 °C. Based on three replicate measurements, a highest uncertainty of ∼12% was observed in the yield stress data. The dashed lines indicate the power-law scaling $\sigma_y \propto \phi^C$, where C is a power-law exponent and the numbers indicate the fractal dimension d_f as estimated from C, across two unique domains. (c) Variations in critical strain (limit of linearity of the elastic modulus) γ_{cr} of $Ca(OH)_2$ suspensions as a function of solid volume fraction. The highest uncertainty observed was ∼10% for the critical strain data for three replicate measurements. The dashed lines indicate the power-law scaling fits, $\gamma_{cr} \propto \phi^B$ with B being a fitting parameter.

double layer (Debye length is κ^{-1}), ψ is the surface potential, and A is the Hamaker constant. The Debye length was estimated as $\kappa^{-1} = \sqrt{\left(\frac{\epsilon_r \epsilon_0 k_B T}{2000 e^2 I N_A}\right)}$, where k_B, N_A, T, e, and I are the Boltzmann constant, Avogadro constant, temperature, elementary charge, and ionic strength of the aqueous medium, respectively. The ionic strength of the medium is estimated as $I = 0.5\sum c_i z_i^2$ with c_i and z_i being the molar concentration and the valence of each ionic species present in the solution. The surface charge, ψ, was approximated from the experimentally determined zeta potential (ζ) value as $\psi = \zeta \exp(\kappa d_s)$,[68] where d_s is the distance from the particle surface to the shear plane (i.e., the plane where the ζ potential is measured and $d_s \approx \kappa^{-1}$).[69] The Hamaker constants for $Ca(OH)_2$ particles at different temperatures were calculated using Lifshitz theory,[68] $A = 1.75 \times 10^{-20}$ J, 1.77×10^{-20} J, and 1.79×10^{-20} J for 25, 50 and 75 °C, respectively.

Figure 2b displays the interparticle interaction potentials for $Ca(OH)_2$ particles suspended in a saturated $Ca(OH)_2$ solution at 25, 50, and 70 °C. The primary repulsive maximum (i.e., energy barrier for particle collisions) decreased with increasing temperature because of decreased electrostatic repulsion between the particles. Colliding particles thus require less kinetic energy to overcome the collision energy barrier, while the collision frequency increases, resulting in a higher rate of agglomeration.[36] For a given $\dot{\gamma}$, the hydrodynamic force per unit area scales as $F_h \propto \eta_0 \dot{\gamma}$[70] and an increase in temperature weakens the hydrodynamic force because the viscosity of the suspending solution decreases. The reduction in the hydrodynamic forces tends to shift the dynamic equilibrium between shear-induced aggregate breakup and colloidal interactions and enhances the formation of aggregates.[32] The V_{vdW} potential that holds the particles together in the aggregates exhibits a weak temperature dependence. With the increase in temperature, the short-range V_{vdW} strength decreased moderately, while the weakened electrostatic repulsion resulted in a reduction in the energy barrier, promoting a higher rate of agglomeration. Higher energy was required to disrupt the aggregate network structure at higher temperatures. The crossover energy, described as the energy required to break down the floc structure and bring a solidlike to liquidlike transition in the suspension rheological response (estimated as $E_{cr} = \int_{0.001}^{\gamma^*} \gamma G' d\gamma$, where γ^* is the crossover strain where the dynamic elastic modulus is equal to the loss modulus, $G' = G''$), increased with temperature (see Figure S6 in the Supporting Information). It should be further noted that, however, when hydrodynamic forces prevail over interparticle interactions, the decrease in the solution viscosity compensates for and masks the effect of particle agglomeration, resulting in the more traditional observation of a decrease in apparent viscosity with an increase in temperature.[40] Hence, it is evident that the interparticle interactions primarily govern the temperature-dependent viscosity responses of $Ca(OH)_2$ suspensions.

In addition to interparticle interactions and particle aggregation, the reprecipitation of dissolved $Ca(OH)_2$ could occur on the surfaces of suspended $Ca(OH)_2$ particles at elevated temperatures, thereby further reducing the interparticle spacing and enhancing aggregation tendencies. However, the increased particle volume fraction was estimated as $\Delta\phi \leq 0.02\%$ (estimated based on the temperature-solubility data), suggesting that its contribution to the rheology is negligible as compared to other factors. Interestingly, modest irreversibility in rheology was observed as the heated suspensions were cooled down to their initial temperature (see Figure S7 in the Supporting Information). This suggests that the microstructural changes that were induced at higher temperatures were not completely reversible upon cooling, as evidenced by the stronger linkage between aggregates as quantified by the crossover energy of the suspensions (see Figure S7 in the Supporting Information).

The aggregate growth rate in suspension was determined using DLS measurements in dilute suspensions (Figure 2c). Aggregate growth rates were accelerated at higher temperatures and for larger particles ($d_{50} = 9.1$ μm). The normalized "Z-average" size (intensity-based overall mean aggregate size) a_z/a_{Z_0} followed a power-law evolution, $a_z/a_{Z_0} \propto t^{\alpha}$, where a_{Z_0} is the initial aggregate size and α is the power-law exponent, which is related to the sticking efficiency among particles (Figure 2c). A larger α indicates faster aggregation kinetics and

https://dx.doi.org/10.1021/acs.langmuir.0c01798
Langmuir 2020, 36, 10811−10821

stronger aggregates.[71] As shown in Figure 2c, α in $Ca(OH)_2$ suspensions was found to increase with temperature. In agreement with apparent viscous activation energy trends, the larger $Ca(OH)_2$ particles exhibited a larger α, which suggests a higher aggregation tendency for these particles. The power-law exponent α can be related to the fractal dimension d_f of the aggregates as $\alpha = z/d_f$ where the value of z is related to the aggregation mechanism.[71,72] For diffusion-limited aggregation, $z = 1$ and $d_f \sim 1.8$, essentially yielding $\alpha \sim 0.55$ (i.e., $a_z/a_{z_0} \sim t^{0.55}$).[72] For aggregate growth controlled by reaction-limited processes, $d_f \geq 2.1$ and $z < 1$, resulting in $\alpha < 0.48$. The α values obtained suggest primarily the reaction-limited aggregation mechanism for $Ca(OH)_2$ particles.

In general, the rate constant for aggregate growth in an electrostatically stabilized suspension can be expressed as $k \propto (k_BT/\eta_0) \exp(-U_{max}/k_BT)$, where U_{max} is the barrier potential.[36,73,74] The rate constant exhibits an inverse exponential dependence on U_{max} and an inverse linear dependence on η_0. Alternately, the apparent aggregation growth rate constant can be approximated from the initial rate of change of effective floc size in DLS measurements as $(da_Z/dt)_{t\to 0} \sim kN_0$.[73,75] Here, N_0 is the initial number-weighted particle concentration that can be estimated from the initial particle concentration C_0 as $N_0 = 3C_0/4\pi a^3\rho$, where ρ is the density of particles. $(da_Z/dt)_{t\to 0}$ was estimated from the initial slopes of the floc size−time data, and the estimated apparent rate constants for the particles at 25 and 70 °C were $\sim 8.9 \times 10^{-14}$ and $\sim 3.0 \times 10^{-13}$ m^3/s, respectively, for smaller $Ca(OH)_2$ particles and $\sim 4.8 \times 10^{-13}$ and $\sim 8.3 \times 10^{-13}$ m^3/s, respectively, for the larger particles. Thus, the estimated aggregation rate constants clearly suggest an increase in aggregation tendency with the increase in temperature.

Influence of the Solid Volume Fraction. The influence of temperature on the suspension's viscosity diminished with increasing particle volume fraction ϕ (Figures 1a and S3). This is manifested in the decreasing apparent viscous activation energy E_a with increasing ϕ (Figure 3a) and is hypothesized to arise from the emergence of particle size-independent aggregate microstructures at high ϕ. These trends were also mirrored in the evolution of the yield stress σ_y with ϕ (Figure 3b). The strain corresponding to the end of the linear viscoelastic regime, wherein the elastic modulus is ~20% lower than the plateau value in the viscoelastic regime, was considered as the critical strain γ_{cr}, and stress corresponding to γ_{cr} was identified as yield stress σ_y. As such, σ_y exhibited a power-law behavior ($\sigma_y \propto \phi^C$) with two distinct ϕ domains bearing different power-law exponents. The power-law scaling of the exponent C is related to the fractal dimension of the flocs within the fractal elasticity model[24,76,77] as $C = (d - 1)/(d - d_f)$, where d represents the Euclidean dimension—i.e., $d = 3$ for three-dimensional spaces.[77,78] Below the transition volume fraction $\phi_T < \sim 0.25$, suspensions of both the particle sizes exhibited similar fractal dimensions, $d_{f,4.6\mu m} = 2.59$ and $d_{f,9.1\mu m} = 2.65$ at 25 °C. However, suspensions comprising larger particles exhibited a significantly lower σ_y (i.e., consistent with lower η, Figure 1b) when compared to suspensions comprising smaller particles. This can be attributed to the somewhat lower specific surface area of the larger $Ca(OH)_2$ particles and their larger interparticle spacings.

Above the transition volume fraction, however, σ_y exhibited a stronger dependence on ϕ, and the difference in σ_y of the suspensions across particle sizes diminished. For example, both suspensions exhibited identical but higher fractal dimensions ($d_{f,4.6\mu m} = 2.82$ and $d_{f,9.1\mu m} = 2.88$) above the transition volume fraction (i.e., when $\phi > \phi_T$) wherein the larger d_f values at higher ϕ are attributed to the more crowded and denser structure of the flocs.[73] This transition in power-law behavior is consistent with the transition from strong-link to weak-link behavior with increasing ϕ as per the fractal elasticity model.[24,77] The model assumes a strong-link behavior at low ϕ where the interfloc links are stronger than the intrafloc links, and consequently, the macroscopic elastic and yielding characteristics are primarily governed by the yielding of intrafloc links. The scaling relation proposed by the fractal theory $\phi = \phi_0(R/a)^{-(d-d_f)}$ can be used to estimate the typical floc to particle size ratio, R/a (where flocs are assumed to be the smallest spheres enclosing the clusters) at different ϕ values.[20,78] Here, ϕ_0 is the maximum packing fraction (i.e., $\phi_0 = 0.64$, for random close packing). Using the d_f values, $R/a = 92, 201$ for the extreme value of the strong-link regime (i.e., $\phi = 0.1$) and $R/a = 67, 156$ for the extreme value of the weak-link regime (i.e., $\phi = 0.3$), for the two $Ca(OH)_2$ particulates with $d_{50} = 4.6$ and 9.1 μm. As ϕ increases, the flocs get smaller and stronger because of the volumetric crowding of the particles and suspensions may cross over to a weak-link regime, wherein the flocs are more rigid than the interfloc links and suspension yielding primarily relies on the interfloc links.[24,77]

As ϕ increases further in the weak-link regime, the flocs become more crowded and the weak interfloc links diminish gradually and the geometric resistance due to the aggregate crowding prevails over weak interfloc links.[79] When the effect of geometric resistance to deformation of the aggregate network becomes pronounced, additional energy is required to push the aggregates away from each other in addition to the energy required to break the interfloc and intrafloc links.[14,79] The fractal elasticity model predicts γ_{cr} to scale with ϕ as $\gamma_{cr} \propto \phi^B$, where the power-law scaling exponent $B = -(1 + x_f)/(d - d_f)$ for the strong-link regime and $B = 1/(d - d_f)$ for the weak-link regime, where x_f is the fractal dimension of the particle chains and is often assumed to be in the range of 1−1.3. Thus, γ_{cr} is expected to exhibit nonmonotonic behavior, that is, an initial decrease in γ_{cr} with increasing ϕ in the strong-link regime and a transition to γ_{cr} increasing with increasing ϕ in the weak-link regime. Indeed, across particle sizes and temperatures, γ_{cr} exhibited a distinct minimum around ϕ_T, confirming this transition in concentrated portlandite suspensions (Figure 3c).

The influence of temperature on the suspension rheology can be rationalized via the fractal elasticity model. As indicated in Figure 3b, the impact of increased temperature on the fractal nature of the aggregates is more evident in the strong-link (lower ϕ) regime. Thus, $d_{f,4.6\mu m}$ decreased from 2.59 to 2.47, indicating the formation of more open flocs. In the weak-link regime (higher ϕ), $d_{f,4.6\mu m}$ remained unchanged at 2.82, suggesting a negligible impact of temperature on the aggregates at higher ϕ. The increasing temperature was shown to increase the aggregation tendencies of the $Ca(OH)_2$ particles, leading to faster aggregation and more open aggregates (Figures 2c and 3b). As such, the effect of temperature on suspension microstructure results in stronger intrafloc links. However, in the weak-link regime, where the flocs are originally rigid and crowded because of higher ϕ, the effect of temperature in modifying the suspension microstructure is subdued. Therefore, the decrease in E_a with increasing ϕ can be ascribed to the

https://dx.doi.org/10.1021/acs.langmuir.0c01798
Langmuir 2020, 36, 10811−10821

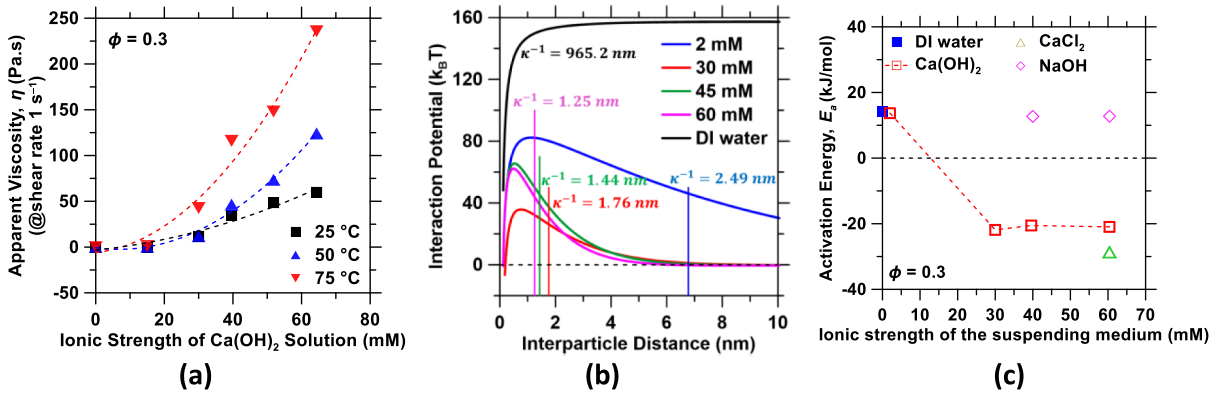

Figure 4. (a) Viscosity of quartz suspensions (ϕ = 0.3) at a shear rate of 1 s^{-1} as a function of the ionic strength of the suspending $Ca(OH)_2$ solution at 25, 50, and 75 °C. An uncertainty of ≤15% was observed in the apparent viscosity data based on three replicate measurements; (b) sphere−sphere DLVO interaction potential as a function of the surface−surface separation distance for quartz particles in different suspending media. The estimated interparticle potentials are based on the electrostatic and van der Waals interactions for 100 nm diameter quartz particles suspended in DI water and $Ca(OH)_2$ solutions having different ionic strengths at 25 °C; (c) estimated apparent activation energy for quartz suspensions (ϕ = 0.3) in different suspending media as a function of their ionic strength. The suspending medium comprising different electrolytes are indicated by different colored data points.

weakened impact of temperature on the aggregation state in the weak-link regime. Thus, the internal structural changes with increasing ϕ explain the reduction in the apparent activation energy of viscous flow, in Figure 3a.

Effects of Ionic Strength and Ion Valence of the Suspending Medium. Interparticle interactions are primarily controlled by the particle's zeta potential and the ionic strength of the suspending medium, which, in turn, control the aggregation state. It is imperative to assess the role of the suspending medium attributes (i.e., pH, ionic strength, and ion valance of the electrolyte) and the resulting particle aggregation state in governing the temperature−viscosity responses of a suspension. These insights can further be used to tailor the temperature-responsive rheological responses of suspensions. On account of their modest solubility and rapid dissolution rate, $Ca(OH)_2$ solutions self-regulate their pH and, hence, it is difficult to control the pH and ionic strength of $Ca(OH)_2$ suspensions at a given temperature. Therefore, experiments were conducted with quartz particulates to elucidate the influences of the suspending medium properties on temperature-dependent viscosity. Quartz was chosen because of its inert nature and very low dissolution rate.

Viscosity of quartz suspensions was found to increase with the ionic strength of suspending $Ca(OH)_2$ solutions (Figure 4a). The higher ionic strength compressed the EDL, thereby leading to a stronger screening of electrostatic repulsion forces, which results in a sharp increase in the viscosity and yield stress of the suspension.[60] The zeta potential measurements indicated that the surface charge of the suspended quartz particles was affected by Ca^{2+} ions in the solution. Quartz particles exhibited $\zeta = -24 \pm 2$ mV when dispersed in DI water and showed a charge reversal in $Ca(OH)_2$ solution even at $I \approx 15$ mM. Furthermore, ζ increased with the $Ca(OH)_2$ concentration in the solution and plateaued around 22 ± 2 mV for I greater than ∼40 mM (see Figure S9 provided in the Supporting Information). The surface charge inversion of quartz particles in $Ca(OH)_2$ solution can occur either due to the adsorption of Ca^{2+} ions to negatively charged quartz surfaces or as a result of ion−ion correlations in the presence of divalent counterions (i.e., Ca^{2+} ions), that is, even without specific adsorption[80,81]

Furthermore, the net interaction potentials between quartz particles dispersed in $Ca(OH)_2$ solutions of varying ionic strength were estimated to assess the impact of the suspending medium on the interparticle interactions (Figure 4b). It should be noted that the ion−ion correlation effect could become significant in the presence of the divalent Ca^{2+} counterions in the suspending medium and hence could induce an additional attraction between the quartz particles.[82] The classical DLVO model does not account for the ion−ion correlation effects; however, its scope can be extended to systems with multivalent counterions by introducing a non-DLVO attractive force term that captures the additional interactions.[83,84] Herein, the interaction potential of quartz particles was estimated using a DLVO model similar to the one used for portlandite particles that did not consider ion−ion correlation effects. Although, ion−ion correlation effects can lead to a more effective electrostatic charge screening and reduction in the energy barrier for quartz particles dispersed in $Ca(OH)_2$ solution, the overall trends in the interaction potential would remain unchanged.

The Debye length was estimated for different suspending media based on their I, and the Hamaker constant was estimated using Lifshitz theory, $A = 1.35 \times 10^{-20}$ J. The Debye length decreased to 1.2 nm in the saturated $Ca(OH)_2$ solution as opposed to being 965 nm in DI water (i.e., assuming pH 7 and $I = 10^{-7}$ M). Correspondingly, the interparticle interactions between quartz particles weakened and the potential barrier U_{max} dropped from ∼157 k_BT in DI water to ∼60 k_BT in saturated $Ca(OH)_2$ solution (Figure 4b). It is notable that the smallest barrier potential was observed at I = 30 mM and increased at higher I. This can be attributed to the competing effects of ζ and I on the interaction potential. Both the Debye length and barrier potential affect the dispersion state of the quartz particles in the suspension. Thus, although quartz particles suspended in DI water are relatively stable against aggregation, they aggregate moderately in $Ca(OH)_2$ solutions. As such, increasing the solution's ionic strength results in increasing the propensity for aggregation so that the suspension tends to exhibit higher viscosities and yield stresses.

The temperature dependence of quartz suspension viscosity was found to vary with the suspending medium. The viscosity

https://dx.doi.org/10.1021/acs.langmuir.0c01798
Langmuir 2020, 36, 10811−10821

of quartz suspensions in DI water decreased with increasing temperature; quartz suspensions in DI water typically exhibited positive viscous activation energies. With increasing $Ca(OH)_2$ ionic strength, from 2 to 30 mM, the activation energy of quartz suspensions decreased and an anomalous transition from positive to negative values emerged (Figure 4c, see also Figures S9). The apparent activation energy remained unaffected ($E_a \cong -20.5 \pm 1$ kJ/mol) in the range 30 mM $\leq I \leq$ 60 mM. To better understand the impact of counterion valence on the temperature dependence of suspension viscosity, quartz suspensions ($\phi = 0.3$) were prepared in NaOH solution (pH ∼ 12.8) and $CaCl_2$ solution (pH ∼ 6.8) featuring an identical ionic strength ($I \sim 60$ mM) as saturated $Ca(OH)_2$ solution and also in NaOH solution of identical pH (pH ∼ 12.6, $I \sim 40$ mM) as that of saturated $Ca(OH)_2$ solution (Figure 4c, see also Figure S9). Quartz suspensions in NaOH exhibited positive activation energy for viscous flow (similar to water), whereas $CaCl_2$ solutions produced negative activation energy (Figure 4c). The sharp increase in the apparent viscosity and the apparent activation energy trends indicate that the quartz particles rapidly flocculate in $Ca(OH)_2$ and $CaCl_2$ solutions as compared to the suspensions in DI water and NaOH solutions. The decrease in viscosity with increasing temperature displayed by quartz suspensions in DI water and NaOH solution implies that water—the suspending medium—governs the suspension viscosity and masks the impact of temperature on the aggregation state of particles, even if there is any. The introduction of divalent cations, Ca^{2+} in the $Ca(OH)_2$ and $CaCl_2$ solutions, modifies the surface charge density of the quartz particles, while compressing the EDL and producing charge reversals, thereby screening the electrostatic repulsions and inducing particle aggregation. The increase in apparent viscosity with increasing temperature exhibited by quartz suspensions in $Ca(OH)_2$ and $CaCl_2$ solutions can be attributed to the higher degree of agglomeration at elevated temperatures. Hence, for these quartz suspensions, similar to the $Ca(OH)_2$ suspensions, the temperature dependence of rheological properties is primarily controlled by interparticle interactions rather than by the rheological properties of the suspending medium.

SUMMARY AND CONCLUSIONS

This study has elucidated the mechanisms that control the temperature-dependent rheological behavior of $Ca(OH)_2$ suspensions, which present high ionic strength and strong charge screening behaviors. A special focus has been placed on identifying the impact of temperature on the interparticle interactions, fractal structuring, and aggregation kinetics of the suspensions. Unlike the suspending medium of saturated $Ca(OH)_2$ solution, the viscosity of dense $Ca(OH)_2$ suspensions increased with increasing temperature, featuring an anomalous "negative" effective activation energy for viscous flow. Increasing temperature was shown to weaken the electrostatic repulsion, leading to faster aggregation and the formation of larger aggregates, which manifests itself in the unusual rheological response of these $Ca(OH)_2$ suspensions with increasing temperature. The impact of temperature on the fractal structure of aggregates was evident in low volume fractions in the strong-link regime wherein branched flocs (i.e., more open structure) were formed, but weakened at higher volume fractions in the weak-link regime featuring densely packed flocs. Furthermore, it was shown that the suspending medium attributes (i.e., ionic strength and ion valance of the electrolyte) and the resulting interparticle interactions can modify the temperature−viscosity responses of a suspension. This study provides insights into aggregation processes that affect the temperature-dependent rheology of suspensions that feature strong charge screening behavior. For example, while processing concentrated cementitious suspensions and other particulate mineral suspensions in highly alkaline media, which are subjected to varying processing temperatures, the temperature-induced modification in the suspension rheology can be crucial and can impact processability. Insights from the present study offer guidance toward the design of suspensions with tailored temperature-dependent and temperature-responsive rheological responses.

ASSOCIATED CONTENT

Supporting Information

The Supporting Information is available free of charge at https://pubs.acs.org/doi/10.1021/acs.langmuir.0c01798.

Particle size distribution, electron microscopy images, flow curves of $Ca(OH)_2$ suspensions, Arrhenius plots of viscosity for $Ca(OH)_2$ suspensions, apparent activation energy as a function of applied shear rate and Mason number, amplitude sweep curves, crossover energy, variations in pH and ionic strength of saturated $Ca(OH)_2$ solution as a function of temperature, zeta potential of quartz particles suspended in $Ca(OH)_2$ solutions, and Arrhenius plots of viscosity for quartz suspensions (PDF)

AUTHOR INFORMATION

Corresponding Author

Gaurav Sant − *Laboratory for the Chemistry of Construction Materials (LC2), Department of Civil and Environmental Engineering, Institute for Carbon Management (ICM), Department of Materials Science and Engineering, and California Nanosystems Institute (CNSI), University of California, Los Angeles, California 90095, United States;* orcid.org/0000-0002-1124-5498; Phone: (310) 206-3084; Email: gsant@ucla.edu

Authors

Sharu Bhagavathi Kandy − *Laboratory for the Chemistry of Construction Materials (LC2), Department of Civil and Environmental Engineering and Institute for Carbon Management (ICM), University of California, Los Angeles, California 90095, United States;* orcid.org/0000-0001-9939-8239

Iman Mehdipour − *Laboratory for the Chemistry of Construction Materials (LC2), Department of Civil and Environmental Engineering and Institute for Carbon Management (ICM), University of California, Los Angeles, California 90095, United States*

Narayanan Neithalath − *School of Sustainable Engineering and the Built Environment, Arizona State University, Tempe, Arizona 86587, United States*

Mathieu Bauchy − *Institute for Carbon Management (ICM) and Laboratory for the Physics of AmoRphous and Inorganic Solids (PARISlab), Department of Civil and Environmental Engineering, University of California, Los Angeles, California 90095, United States;* orcid.org/0000-0003-4600-0631

Edward Garboczi − *Applied Chemicals and Materials Division, Material Measurement Laboratory, National Institute of*

https://dx.doi.org/10.1021/acs.langmuir.0c01798
Langmuir 2020, 36, 10811−10821

Standards and Technology, Boulder, Colorado 80305, United States

Samanvaya Srivastava − *Institute for Carbon Management (ICM) and Department of Chemical and Biomolecular Engineering, University of California, Los Angeles, California 90095, United States;* orcid.org/0000-0002-3519-7224

Torben Gaedt − *Department of Chemistry, Technische Universität München, 85747 Garching, Germany*

Complete contact information is available at: https://pubs.acs.org/10.1021/acs.langmuir.0c01798

Notes

The authors declare no competing financial interest.

■ ACKNOWLEDGMENTS

The authors acknowledge the financial support for this research from the National Science Foundation (DMREF: 1922167), Department of Energy: Office of Fossil Energy via the National Energy Technology Laboratory (DE-FE0031718), and TRANSCEND: a joint UCLA-NIST Consortium that is funded by its industry and agency partners. This research was conducted in the Laboratory for the Chemistry of Construction Materials (LC^2) and the Electron Microscopy Core Facility at UCLA. As such, the authors gratefully acknowledge the support provided by these laboratories that has made operations possible. The contents of this paper reflect the views and opinions of the authors, who are responsible for the accuracy of the data sets presented herein, and do not reflect the views and/or policies of the funding agencies nor do the contents constitute a specification, standard, or regulation.

■ ADDITIONAL NOTES

[a]Certain commercial equipment, software, and/or materials are identified in this paper in order to adequately specify the experimental procedure. In no case does such identification imply recommendation or endorsement by the National Institute of Standards and Technology nor does it imply that the equipment and/or materials used are necessarily the best available for the purpose.

[b]This more dilute condition was chosen to mitigate issues associated with multiple scattering from (multiple) proximate particles. In spite of the lower particle volume used for this volume fraction, the (centroid-to-centroid) interparticle spacing computed using the median particle size (d_{50} = 4.6 μm) in a uniformly dispersed suspension is around 136.6 μm. On the other hand, for ϕ = 0.45, for the same median particle size, the interparticle spacing in a uniformly dispersed suspension is around 4.8 μm. Thus, a 225x increase in solid loading produces a 28.5x reduction in the particle spacing. Although this is an idealized approximation for monodisperse particles, given the small screening lengths of portlandite suspensions, it supports the selection of more dilute suspensions for the DLS analyses to assess the aggregation behavior of more concentrated suspensions.

■ REFERENCES

(1) Larson, R. G. *The Structure and Rheology of Complex Fluids*; Oxford University Press, 1999.

(2) Blanco, E.; Hodgson, D. J. M.; Hermes, M.; Besseling, R.; Hunter, G. L.; Chaikin, P. M.; Cates, M. E.; Van Damme, I.; Poon, W. C. K. Conching Chocolate Is a Prototypical Transition from Frictionally Jammed Solid to Flowable Suspension with Maximal Solid Content. *Proc. Natl. Acad. Sci. U.S.A.* **2019**, *116*, 10303−10308.

(3) Martínez-Bustos, F.; Chang, Y. K.; Bannwart, A. C.; Rodríguez, M. E.; Guedes, P. A.; Gaiotti, E. R. Effects of Calcium Hydroxide and Processing Conditions on Corn Meal Extrudates. *Cereal Chem.* **1998**, *75*, 796−801.

(4) Ruiz-Agudo, E.; Rodriguez-Navarro, C. Microstructure and Rheology of Lime Putty. *Langmuir* **2010**, *26*, 3868−3877.

(5) Tseng, W. J.; Wu, C. H. Aggregation, rheology and electrophoretic packing structure of aqueous A12O3 nanoparticle suspensions. *Acta Mater.* **2002**, *50*, 3757−3766.

(6) Savarmand, S.; Carreau, P. J.; Bertrand, F.; Vidal, D. J.-E.; Moan, M. Rheological Properties of Concentrated Aqueous Silica Suspensions: Effects of PH and Ions Content. *J. Rheol.* **2003**, *47*, 1133−1149.

(7) Lewis, J. A. Colloidal Processing of Ceramics. *J. Am. Ceram. Soc.* **2004**, *83*, 2341−2359.

(8) Kelessidis, V. C.; Maglione, R.; Tsamantaki, C.; Aspirtakis, Y. Optimal Determination of Rheological Parameters for Herschel-Bulkley Drilling Fluids and Impact on Pressure Drop, Velocity Profiles and Penetration Rates during Drilling. *J. Pet. Sci. Eng.* **2006**, *53*, 203−224.

(9) Feilden, E.; Ferraro, C.; Zhang, Q.; García-Tuñón, E.; D'Elia, E.; Giuliani, F.; Vandeperre, L.; Saiz, E. 3D Printing Bioinspired Ceramic Composites. *Sci. Rep.* **2017**, *7*, 13759.

(10) Roussel, N. Rheological Requirements for Printable Concretes. *Cem. Concr. Res.* **2018**, *112*, 76−85.

(11) De Schutter, G.; Lesage, K.; Mechtcherine, V.; Nerella, V. N.; Habert, G.; Agusti-Juan, I. Vision of 3D printing with concrete - Technical, economic and environmental potentials. *Cem. Concr. Res.* **2018**, *112*, 25−36.

(12) Dudukovic, N. A.; Wong, L. L.; Nguyen, D. T.; Destino, J. F.; Yee, T. D.; Ryerson, F. J.; Suratwala, T.; Duoss, E. B.; Dylla-Spears, R. Predicting Nanoparticle Suspension Viscoelasticity for Multimaterial 3D Printing of Silica-Titania Glass. *ACS Appl. Nano Mater.* **2018**, *1*, 4038−4044.

(13) Kang, H.-W.; Lee, S. J.; Ko, I. K.; Kengla, C.; Yoo, J. J.; Atala, A. A 3D Bioprinting System to Produce Human-Scale Tissue Constructs with Structural Integrity. *Nat. Biotechnol.* **2016**, *34*, 312−319.

(14) Mewis, J.; Wagner, N. J. *Colloidal Suspension Rheology*; Cambridge University Press, 2012.

(15) Mueller, S.; Llewellin, E. W.; Mader, H. M. The Rheology of Suspensions of Solid Particles. *Proc. R. Soc. A* **2010**, *466*, 1201−1228.

(16) Leong, Y.-K.; Scales, P. J.; Healy, T. W.; Boger, D. V. Effect of Particle Size on Colloidal Zirconia Rheology at the Isoelectric Point. *J. Am. Ceram. Soc.* **1995**, *78*, 2209−2212.

(17) Zhou, Z.; Scales, P. J.; Boger, D. V. Chemical and Physical Control of the Rheology of Concentrated Metal Oxide Suspensions. *Chem. Eng. Sci.* **2001**, *56*, 2901−2920.

(18) Scales, P. J.; Johnson, S. B.; Healy, T. W.; Kapur, P. C. Shear Yield Stress of Partially Flocculated Colloidal Suspensions. *AIChE J.* **1998**, *44*, 538−544.

(19) Flatt, R. J.; Bowen, P. Yodel: A Yield Stress Model for Suspensions. *J. Am. Ceram. Soc.* **2006**, *89*, 1244−1256.

(20) Genovese, D. B. Shear Rheology of Hard-Sphere, Dispersed, and Aggregated Suspensions, and Filler-Matrix Composites. *Adv. Colloid Interface Sci.* **2012**, *171−172*, 1−16.

(21) Tadros, T. F. *Polymeric Surfactants: Dispersion Stability and Industrial Applications*; Walter de Gruyter GmbH, 2017.

(22) Hunter, R. J.; Nicol, S. K. The Dependence of Plastic Flow Behavior of Clay Suspensions on Surface Properties. *J. Colloid Interface Sci.* **1968**, *28*, 250−259.

(23) Firth, B. A.; Hunter, R. J. Flow Properties of Coagulated Colloidal Suspensions. *J. Colloid Interface Sci.* **1976**, *57*, 266−275.

(24) Shih, W. Y.; Shih, W.-H.; Aksay, I. A. Elastic and Yield Behavior of Strongly Flocculated Colloids. *J. Am. Ceram. Soc.* **1999**, *82*, 616−624.

(25) Gossard, A.; Frances, F.; Aloin, C. Rheological Properties of TiO2 Suspensions Varied by Shifting the Electrostatic Inter-Particle

Interactions with an Organic Co-Solvent. *Colloids Surf., A* **2017**, *522*, 425−432.
(26) Wang, X.; Sun, Y.; Peng, C.; Luo, H.; Wang, R.; Zhang, D. Transitional Suspensions Containing Thermosensitive Dispersant for Three-Dimensional Printing. *ACS Appl. Mater. Interfaces* **2015**, *7*, 26131−26136.
(27) Rocha, V. G.; García-Tuñón, E.; Botas, C.; Markoulidis, F.; Feilden, E.; D'Elia, E.; Ni, N.; Shaffer, M.; Saiz, E. Multimaterial 3D Printing of Graphene-Based Electrodes for Electrochemical Energy Storage Using Thermoresponsive Inks. *ACS Appl. Mater. Interfaces* **2017**, *9*, 37136−37145.
(28) Chen, X.; Wang, C.; Wang, Y.; Wang, H.; Wang, R. Prevention Strategy of Cement Slurry Sedimentation under High Temperature. Part 1: A Polymer with Continuous Thermo-Thickening Behavior from 48 to 148 °C. *J. Phys. Chem. C* **2019**, *123*, 18573−18584.
(29) Pagnoux, C.; Serantoni, M.; Laucournet, R.; Chartier, T.; Baumard, J.-F. Influence of the Temperature on the Stability of Aqueous Alumina Suspensions. *J. Eur. Ceram. Soc.* **1999**, *19*, 1935−1948.
(30) Yamaguchi, K.; Senna, M.; Kuno, H. Effect of temperature on the flow properties of suspensions. *J. Colloid Interface Sci.* **1979**, *70*, 584−591.
(31) Maron, S. H.; Pierce, P. E. Application of Ree-Eyring Generalized Flow Theory to Suspensions of Spherical Particles. *J. Colloid Sci.* **1956**, *11*, 80−95.
(32) Tsutsumi, A.; Yoshida, K. Effect of Temperature on Rheological Properties of Suspensions. *J. Non-Newtonian Fluid Mech.* **1987**, *26*, 175−183.
(33) Timmons, J.; Falzone, G.; Balonis, M.; Bauchy, M.; Sant, G. Anomalous Variations in the Viscous Activation Energy of Suspensions Induced by Fractal Structuring. *J. Colloid Interface Sci.* **2018**, *530*, 603−609.
(34) Li, W.; Zhang, Q.; Gu, M.; Jin, Y. Effect of Temperature on Rheological Behavior of Silicon Carbide Aqueous Suspension. *Ceram. Int.* **2006**, *32*, 761−765.
(35) Amiri, A.; Øye, G.; Sjöblom, J. Temperature and Pressure Effects on Stability and Gelation Properties of Silica Suspensions. *Colloids Surf., A* **2011**, *378*, 14−21.
(36) Reerink, H.; Overbeek, J. T. G. The Rate of Coagulation as a Measure of the Stability of Silver Iodide Sols. *Discuss. Faraday Soc.* **1954**, *18*, 74−84.
(37) Garciagarcia, S.; Wold, S.; Jonsson, M. Effects of Temperature on the Stability of Colloidal Montmorillonite Particles at Different PH and Ionic Strength. *Appl. Clay Sci.* **2009**, *43*, 21−26.
(38) Kim, D. C.; Kang, M. H.; Choi, C. K.; Ryu, J. Y.; Kim, D. L.; Lim, T. K. Temperature Effect on the Kinetics of the Polystyrene Aggregation Progress by Using Static and Dynamic Light Scatterings. *J. Korean Phys. Soc.* **1997**, *31*, 271−276.
(39) Shu, R.; Sun, W.; Liu, X.; Tong, Z. Temperature Dependence of Aging Kinetics of Hectorite Clay Suspensions. *J. Colloid Interface Sci.* **2015**, *444*, 132−140.
(40) Tarì, G.; Olhero, S. M.; Ferreira, J. M. F. Influence of Temperature on Stability of Electrostatically Stabilized Alumina Suspensions. *J. Colloid Interface Sci.* **2000**, *231*, 221−227.
(41) Wang, X.; Guo, L. Effect of Temperature on the Stability of Aqueous ZrO2 Suspensions. *Colloids Surf., A* **2007**, *304*, 1−6.
(42) Chandler, H. D. Activation entropy and anomalous temperature dependence of viscosity in aqueous suspensions of Fe 2 O 3. *Powder Technol.* **2017**, *305*, 572−577.
(43) Elert, K.; Rodriguez-Navarro, C.; Pardo, E. S.; Hansen, E.; Cazalla, O. Lime Mortars for the Conservation of Historic Buildings. *Stud. Conserv.* **2002**, *47*, 62−75.
(44) Adroer, M.; Valero, F.; Poch, M.; Solà, C. A New Procedure for Water Decarbonation Process Control. *Ind. Eng. Chem. Res.* **1994**, *33*, 1501−1509.
(45) Lim, S.; Jeon, W.; Lee, J.; Lee, K.; Kim, N. Engineering Properties of Water/Wastewater-Treatment Sludge Modified by Hydrated Lime, Fly Ash and Loess. *Water Res.* **2002**, *36*, 4177−4184.
(46) Murray, P. E.; Hafez, A. A.; Smith, A. J.; Cox, C. F. Hierarchy of Pulp Capping and Repair Activities Responsible for Dentin Bridge Formation. *Am. J. Dent.* **2002**, *15*, 236−243.
(47) Rodriguez-Navarro, C.; Suzuki, A.; Ruiz-Agudo, E. Alcohol Dispersions of Calcium Hydroxide Nanoparticles for Stone Conservation. *Langmuir* **2013**, *29*, 11457−11470.
(48) Ruiz-Agudo, E.; Kudłacz, K.; Putnis, C. V.; Putnis, A.; Rodriguez-Navarro, C. Dissolution and Carbonation of Portlandite [Ca(OH)2] Single Crystals. *Environ. Sci. Technol.* **2013**, *47*, 11342−11349.
(49) Bates, R. G.; Bower, V. E.; Smith, E. R. Calcium Hydroxide as a Highly Alkaline PH Standard. *J. Res. Natl. Bur. Stand.* **1956**, *56*, 305−312.
(50) Timmons, J.; Mehdipour, I.; Gao, S.; Atahan, H.; Neithalath, N.; Bauchy, M.; Garboczi, E.; Srivastava, S.; Sant, G. Dispersing Nano- and Micro-Sized Portlandite Particulates via Electrosteric Exclusion at Short Screening Lengths. *Soft Matter* **2020**, *16*, 3425−3435.
(51) Delgado, A. V.; González-Caballero, F.; Hunter, R. J.; Koopal, L. K.; Lyklema, J. Measurement and Interpretation of Electrokinetic Phenomena (IUPAC Technical Report). *Pure Appl. Chem.* **2005**, *77*, 1753−1805.
(52) Chandler, H. D. Activation Energy and Entropy for Viscosity of Wormlike Micelle Solutions. *J. Colloid Interface Sci.* **2013**, *409*, 98−103.
(53) Chandler, H. D. An Activation Energy Approach to Analysing Non-Newtonian Slurry Viscosities with Application to a Suspension of Starch in a Carboxymethylcellulose Solution. *Powder Technol.* **2014**, *268*, 368−372.
(54) Rohindra, D. R.; Lata, R. A.; Coll, R. K. A Simple Experiment to Determine the Activation Energy of the Viscous Flow of Polymer Solutions Using a Glass Capillary Viscometer. *Eur. J. Phys.* **2012**, *33*, 1457−1464.
(55) Rubio-Hernández, F. J.; Gómez-Merino, A. I.; Delgado-García, R.; Páez-Flor, N. M. An Activation Energy Approach for Viscous Flow: A Complementary Tool for the Study of Microstructural Evolutions in Sheared Suspensions. *Powder Technol.* **2017**, *308*, 318−323.
(56) Gómez-Merino, A. I.; Arjona-Escudero, J. L.; Santos-Ráez, I. M.; Rubio-Hernández, F. J. Microstructure and Thermodynamic Properties of Aqueous Alumina Nanofluids. *Powder Technol.* **2019**, *353*, 509−515.
(57) Sonntag, R. C.; Russel, W. B. Structure and breakup of flocs subjected to fluid stresses. *J. Colloid Interface Sci.* **1986**, *113*, 399−413.
(58) Wessel, R.; Ball, R. C. Fractal Aggregates and Gels in Shear Flow. *Phys. Rev. A: At., Mol., Opt. Phys.* **1992**, *46*, R3008−R3011.
(59) Leong, Y.-K.; Boger, D. V. Surface Chemistry Effects on Concentrated Suspension Rheology. *J. Colloid Interface Sci.* **1990**, *136*, 249−258.
(60) Johnson, S. B.; Franks, G. V.; Scales, P. J.; Boger, D. V.; Healy, T. W. Surface Chemistry-Rheology Relationships in Concentrated Mineral Suspensions. *Int. J. Miner. Process.* **2000**, *58*, 267−304.
(61) Brady, J. F.; Vicic, M. Normal Stresses in Colloidal Dispersions. *J. Rheol.* **1995**, *39*, 545−566.
(62) Jamali, S.; Armstrong, R. C.; McKinley, G. H. Time-Rate-Transformation Framework for Targeted Assembly of Short-Range Attractive Colloidal Suspensions. *Mater. Today Adv.* **2020**, *5*, 100026.
(63) Varga, Z.; Swan, J. W. Large Scale Anisotropies in Sheared Colloidal Gels. *J. Rheol.* **2018**, *62*, 405−418.
(64) Varga, Z.; Grenard, V.; Pecorario, S.; Taberlet, N.; Dolique, V.; Manneville, S.; Divoux, T.; McKinley, G. H.; Swan, J. W. Hydrodynamics Control Shear-Induced Pattern Formation in Attractive Suspensions. *Proc. Natl. Acad. Sci. U.S.A.* **2019**, *116*, 12193−12198.
(65) Aschauer, U.; Burgos-Montes, O.; Moreno, R.; Bowen, P. Hamaker 2: A Toolkit for the Calculation of Particle Interactions and Suspension Stability and Its Application to Mullite Synthesis by Colloidal Methods. *J. Dispersion Sci. Technol.* **2011**, *32*, 470−479.

https://dx.doi.org/10.1021/acs.langmuir.0c01798
Langmuir 2020, 36, 10811−10821

(66) Hogg, R.; Healy, T. W.; Fuerstenau, D. W. Mutual Coagulation of Colloidal Dispersions. *Trans. Faraday Soc.* **1966**, *62*, 1638−1651.
(67) Hamaker, H. C. The London-van Der Waals Attraction between Spherical Particles. *Physica* **1937**, *4*, 1058−1072.
(68) Israelachvili, J. N. *Intermolecular and Surface Forces*; Academic Press, 2015.
(69) Ding, W.; Liu, X.; Song, L.; Li, Q.; Zhu, Q.; Zhu, H.; Hu, F.; Luo, Y.; Zhu, L.; Li, H. An Approach to Estimate the Position of the Shear Plane for Colloidal Particles in an Electrophoresis Experiment. *Surf. Sci.* **2015**, *632*, 50−59.
(70) Goren, S. L. The Hydrodynamic Forces on Touching Spheres along the Line of Centers Exerted by a Shear Field. *J. Colloid Interface Sci.* **1971**, *36*, 94−96.
(71) Trinh, L. T. T.; Kjøniksen, A.-L.; Zhu, K.; Knudsen, K. D.; Volden, S.; Glomm, W. R.; Nyström, B. Slow Salt-Induced Aggregation of Citrate-Covered Silver Particles in Aqueous Solutions of Cellulose Derivatives. *Colloid Polym. Sci.* **2009**, *287*, 1391−1404.
(72) Pamies, R.; Cifre, J. G. H.; Espín, V. F.; Collado-González, M.; Baños, F. G. D.; De La Torre, J. G. Aggregation Behaviour of Gold Nanoparticles in Saline Aqueous Media. *J. Nanoparticle Res.* **2014**, *16*, 2376.
(73) Metin, C. O.; Bonnecaze, R. T.; Lake, L. W.; Miranda, C. R.; Nguyen, Q. P. Aggregation Kinetics and Shear Rheology of Aqueous Silica Suspensions. *Appl. Nanosci.* **2014**, *4*, 169−178.
(74) Hunter, R. J. *Foundations of Colloid Science*; Oxford University Press, 2001.
(75) Schudel, M.; Behrens, S. H.; Holthoff, H.; Kretzschmar, R.; Borkovec, M. Absolute Aggregation Rate Constants of Hematite Particles in Aqueous Suspensions: A Comparison of Two Different Surface Morphologies. *J. Colloid Interface Sci.* **1997**, *196*, 241−253.
(76) Shih, W.-H.; Shih, W. Y.; Kim, S.-I.; Liu, J.; Aksay, I. A. Scaling behavior of the elastic properties of colloidal gels. *Phys. Rev. A: At., Mol., Opt. Phys.* **1990**, *42*, 4772−4779.
(77) Wu, H.; Morbidelli, M. A Model Relating Structure of Colloidal Gels to Their Elastic Properties. *Langmuir* **2001**, *17*, 1030−1036.
(78) Liberto, T.; Le Merrer, M.; Barentin, C.; Bellotto, M.; Colombani, J. Elasticity and Yielding of a Calcite Paste: Scaling Laws in a Dense Colloidal Suspension. *Soft Matter* **2017**, *13*, 2014−2023.
(79) Zhou, Z.; Solomon, M. J.; Scales, P. J.; Boger, D. V. The Yield Stress of Concentrated Flocculated Suspensions of Size Distributed Particles. *J. Rheol.* **1999**, *43*, 651−671.
(80) Wernersson, E.; Kjellander, R.; Lyklema, J. Charge Inversion and Ion−Ion Correlation Effects at the Mercury/Aqueous MgSO4 Interface: Toward the Solution of a Long-Standing Issue. *J. Phys. Chem. C* **2010**, *114*, 1849−1866.
(81) Kékicheff, P.; Marčelja, S.; Senden, T. J.; Shubin, V. E. Charge Reversal Seen in Electrical Double Layer Interaction of Surfaces Immersed in 2:1 Calcium Electrolyte. *J. Chem. Phys.* **1993**, *99*, 6098−6113.
(82) Misra, R. P.; De Souza, J. P.; Blankschtein, D.; Bazant, M. Z. Theory of Surface Forces in Multivalent Electrolytes. *Langmuir* **2019**, *35*, 11550−11565.
(83) Danov, K.; Basheva, E.; Kralchevsky, P. Effect of Ionic Correlations on the Surface Forces in Thin Liquid Films: Influence of Multivalent Coions and Extended Theory. *Materials* **2016**, *9*, 145.
(84) Moazzami Gudarzi, M.; Trefalt, G.; Szilagyi, I.; Maroni, P.; Borkovec, M. Forces between Negatively Charged Interfaces in the Presence of Cationic Multivalent Oligoamines Measured with the Atomic Force Microscope. *J. Phys. Chem. C* **2015**, *119*, 15482−15490.

https://dx.doi.org/10.1021/acs.langmuir.0c01798
Langmuir 2020, 36, 10811−10821